Dalton Transactions

ROYAL SOCIETY OF CHEMISTRY

COMMUNICATION

View Article Online
View Journal | View Issue

Cite this: *Dalton Trans.*, 2024, **53**, 16815

Received 13th July 2024,
Accepted 26th September 2024

DOI: 10.1039/d4dt02024c

rsc.li/dalton

A 2-fold interpenetrating 3D pillar-layered MOF for the gas separation and detection of metal ions†

Guoqiang Peng,[a] Zhibo Su,[a] Falu Hu, *[a] Zhenyu Ji,[b] Zhengyi Di,[c] Guihua Li,[a] Tingting Gao,[a] Guowei Zhou*[a] and Mingyan Wu *[b]

A 2-fold interpenetrating 3D pillar-layered MOF, which was assembled from a mixed-linker and paddle-wheel cluster, was successfully synthesized. It possesses good thermal and water stability as well as high selectivity for C_2H_6 over CH_4 and CO_2 over N_2 under ambient conditions, which was further proved by breakthrough experiments. Moreover, this porous material exhibits good detection of Cu^{2+}, $[Co(NH_3)_6]^{3+}$ and Fe^{3+} in an aqueous solution.

Metal–organic frameworks (MOFs) feature porous structures constructed from metal ions or clusters and organic ligands, showing significant potential in the field of gas storage and separation.[1–21] Compared to other solid adsorbents such as active carbon and zeolite, MOFs possess a higher surface area, tuneable pore size and easy function, which makes them more suitable candidates for gas storage and separation. Pillar-layered MOFs act as an important branch of Hofmann clathrates, enriching structural diversity and designability, which usually include two different ligands: oxygen-donor and N-donor ligands.[22–35] The introduction of a second ligand may be beneficial for controlling the pore size and enhancing the rigidity of the structure, which could improve the efficiency of gas separation. Recently, some works on gas purification have been reported by our group,[36–44] and we now introduce a Hofmann clathrate structure to achieve the purification of gas.

Based on the above consideration, we demonstrate the synthesis and characterization of mixed-ligand-pillar-layered MOF materials with permanent porosity. The new compound utilizes the robust carboxylate paddle-wheel-type coordination of Zn(II) pairs to form 2D layers that are pillared with nearly linear 4,4′-bipyridine linkages to yield a 2-fold mixed-ligand 3D framework. Furthermore, we explore the separation of C_2H_6 over CH_4 and CO_2 over N_2 using both theoretical calculation and breakthrough experiments. Additionally, we explore the luminescent Zn-MOF for selective recognition of Cu^{2+}, $[Co(NH_3)_6]^{3+}$ and Fe^{3+}.

A 2-fold interpenetrating pillar-layered structure with a paddle-wheel SBU was successfully prepared using $Zn(NO_3)_2{\cdot}6H_2O$, 4,4′,4″,4‴-(thiophene-2,3,4,5-tetrayl)tetrakis(2-fluorobenzoic acid) (H_4tbca-4F) and 4,4′-bipyridine (bpy) under solvothermal conditions. It is noted that a new ligand, 4,4′,4″,4‴-(1-methyl-1*H*-pyrrole-2,3,4,5-tetrayl)tetrakis(2-fluorobenzoic acid) (H_4mpca-4F) is generated within the structure after the solvothermal reaction, which is determined using ESI-MS and single-crystal X-ray diffraction data (Schemes S3 and S4†). The compound can be formulated as Zn_2(tbca-4F)$_{0.733}$(mpca-4F)$_{0.267}$(4,4′-bipyridine)·2DMF (**1**). SCXRD analysis revealed that **1** crystallized in the monoclinic space group *C*2/*m*. In each asymmetric unit, there are 0.733 tbca-4F and 0.267 mpca-4F ligands, one independent Zn(II) ion and half of coordinating bpy (Fig. S1a†). Thus, the metal Zn(II) ions are coordinatively saturated by the tbca-4F, mpca-4F and bpy ligands. In the tbca-4F and mpca-4F ligands, all the four carboxyl groups are fully deprotonated and coordinated to the classical di-nuclear Zn(II) paddlewheel unit, $Zn_2(COO)_4$, through bidentate bridging modes. Therefore, on the whole, **1** is electroneutral. Interestingly, the N atoms of 4,4′-bipyridine occupy the axial position to form the $Zn_2(COO)_4N_2$ unit (Fig. S1b†), which is different from those of the terminal molecules coordinating the axial position of the paddle-wheel SBU. Each Zn^{2+} ion is surrounded by four O atoms from four carboxyl groups and one N atom from the bpy linker, leading to the geometry of the tetragonal pyramid (Fig. S1c†). In the fully deprotonated tbca-4F ligand, the angle of the thiophene ring with outer benzene ring is 58.161° and 80.152°, respectively,

[a]*Key Laboratory of Fine Chemicals in Universities of Shandong, Jinan Engineering Laboratory for Multi-Scale Functional Materials, School of Chemistry and Chemical Engineering, Qilu University of Technology (Shandong Academy of Sciences), Jinan 250353, P. R. China. E-mail: faluhu@qlu.edu.cn, gwzhou@qlu.edu.cn*
[b]*State Key Laboratory of Structure Chemistry, Fujian Institute of Research on the Structure of Matter, Chinese Academy of Sciences, Fuzhou, 350002, P. R. China. E-mail: wumy@fjirsm.ac.cn*
[c]*Tianjin Key Laboratory of Structure and Performance for Functional Molecules, College of Chemistry, Tianjin Normal University, Tianjin 300387, P. R. China*

†Electronic supplementary information (ESI) available: Crystallographic data, additional figures and tables. CCDC 2369823. For ESI and crystallographic data in CIF or other electronic format see DOI: https://doi.org/10.1039/d4dt02024c

while the four C atoms from four COO^- groups are co-planar, resulting in a trapezoidal planar conformation of the tbca-4F ligand. The Zn–O distances are in the range of 1.999–2.114 Å and the Zn–N distance is 2.034 Å.

As shown in Fig. 1, each tbca-4F ligand connects four Zn_2 clusters to form a two-dimensional layered structure with three types of windows (A, B, C). The size of one fusiform aperture (A) is 6.3 (S1–S1) × 16.6 Å (Zn1–Zn1) and the sizes of the other two square windows (B, C) are 9.6 × 9.6 and 10.2 × 8.7 Å between benzenes, respectively. Interestingly, the two remaining axial positions of the $Zn_2(COO)_4$ unit are occupied by N atoms from the 4,4′-bipyridine linkers, which serve as a pillar between the adjacent 2D layers. Thus, the 2D layers were further connected by pillared linkers to form a 3D pillar-layered structure. The single net shows a 1D channel with the size of a window of 11.1 × 12.1 Å along the *b* axis. It is noted that the single 3D net is interpenetrated with the other net to form the 2-fold structure for the 4,4′-bipyridine linkers interpenetrating the square windows C (10.2 × 8.7 Å) and the channel of single net (11.1 × 12.1 Å), which is enough large size to accommodate the 4,4′-bipyridine linker and the paddle-wheel cluster (Fig. S2c†). As the interpenetrating phenomenon, window C was blocked and meanwhile, along the *b*-axis, the channels in each single net are also blocked by the other single net, which both contribute to the tuning of the pore/window sizes. On the whole, in the interpenetrating structure, there exist three different kinds of windows, including the above-mentioned A and B windows and one new D window (6.3 × 9.5 Å; S1–S1 and O4–O4), which result from the interpenetration (Fig. S2a†). In view of topology, the trapezoidal tbca-4F ligand can be acted as a 4-connected node, the paddlewheel cluster $Zn_2(COO)_4N_2$ can be simplified as the 6-connected node and the linear 4,4′-bipyridine ligand can be considered as a linker. Thus, the structure of **1** exhibits a 2-nodal 4,6-connected ***fsc*** topology network with a point symbol of $\{4^4{\cdot}6^{10}{\cdot}8\}\{4^4{\cdot}6^2\}$ by using the TOPOS 4.0 program package (Fig. S3†).[45] The solvent accessible volume in fully evacuated **1** is about 22.9%, which is estimated by PLATON.[46] The PXRD of the bulk fresh sample is well matched with that of the simulated, indicating the phase purity of the bulk samples (Fig. S4†). To evaluate the stability for practical applications, the thermogravimetric analysis (TGA) and variable-temperature PXRD of the activated sample were carried out. The TGA reveals that the activated sample can be stable up to 280 °C (Fig. S5†). The variable-temperature PXRD of the activated sample shows that no obvious changes in the PXRD patterns could be observed even at 180 °C in air atmosphere (Fig. S6†). The above results prove that the activated sample **1a** possesses good thermal stability. On the other hand, after immersing fresh samples in water and various solvents for 24 h, the PXRD patterns maintained sharp peaks, indicating good water and solvent stabilities (Fig. S7†). The high stabilities of **1a** encourage us to explore its applications in solutions and solids.

Considering the pore structure and ultra-high stability, the N_2 adsorption isotherm was collected to confirm the permanent porosity of **1a** at 77 K and 1 bar. Before the gas adsorption experiment, the activated sample was obtained by soaking the fresh sample in MeOH for 3 days and are then heated at 80 °C for 10 h in the dynamic high vacuum. The N_2 adsorption isotherm shows a typical type-I adsorption behaviour, indicating the microporous nature of **1a**. The maximal adsorption capacity is 131.5 $cm^3\ g^{-1}$ with an estimated BET surface area of 446 $m^2\ g^{-1}$ (Fig. S8†). Single-component gas sorption isotherms were collected on the equipment of 3-Flex. The results exhibited 25.5 $cm^3\ g^{-1}$ as an adsorption amount of C_2H_6, while the CH_4 adsorption amount was only 10.5 $cm^3\ g^{-1}$ under 298 K and 1 bar (Fig. 2a). Their adsorption amount difference and C_2H_6/CH_4 uptake ratio are 15 $cm^3\ g^{-1}$ and 243%, respectively. More interestingly, the activated sample saturates with C_2H_6 at lower pressures and the slope of the C_2H_6 adsorption isotherm is much steeper than that of CH_4 indicating the stronger affinity between C_2H_6 and the pore surfaces. Besides, the adsorption isosteric heat (Q_{st}) is calculated by using the Clausius–Clapeyron equation based on the gas adsorption data measured at 273 K and 298 K. The Q_{st} value for C_2H_6 is 24.38 kJ mol^{-1}, which is much higher than that of CH_4 (16.72 kJ mol^{-1}), further confirming the stronger framework–C_2H_6 interaction (Fig. S10†). Such difference in adsorption amounts and the framework–gas interactions for C_2H_6 and CH_4 indicates that **1a** may enable highly selective separations for C_2H_6 from CH_4. Subsequently, the ideal adsorbed solution theory (IAST) was used to predict the selectivity of binary C_2H_6/CH_4 (molar ratios: 15 : 85) based on single-component adsorption data fitting using the dual-site Langmuir Freundlich (DSLF) equation at 298 K. As anticipated, the selectivity of **1a** between C_2H_6 and CH_4 is high, up to 128.5 at the low-pressure regions and decreases to 77.6 at 298 K and 1 bar (Fig. 2b), which is higher than that reported for most adsorbents such as DMOF-$(CF_3)_2$ (15),[47] MIL-126(Fe/Co) (13.2),[48] JUC-220 (46),[49] LIFM-W2 (19),[50] BSF-1 (23),[51] SBMOF-1(74),[52] GNU-1a (17.5),[53]

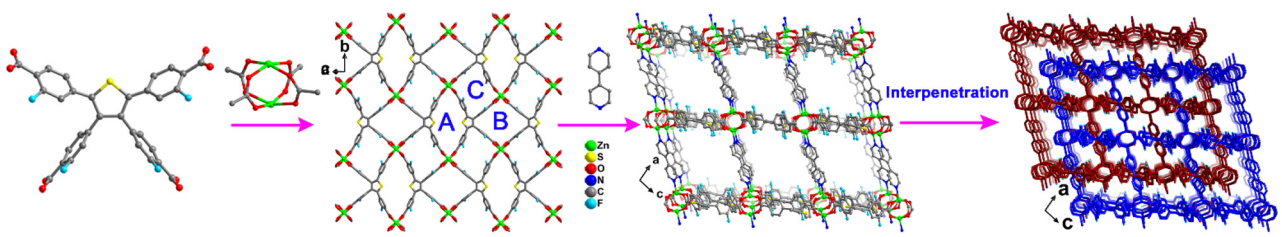

Fig. 1 Views of the tbca-4F ligand, paddle-wheel cluster, 2D layer, single net and 2-fold structure.

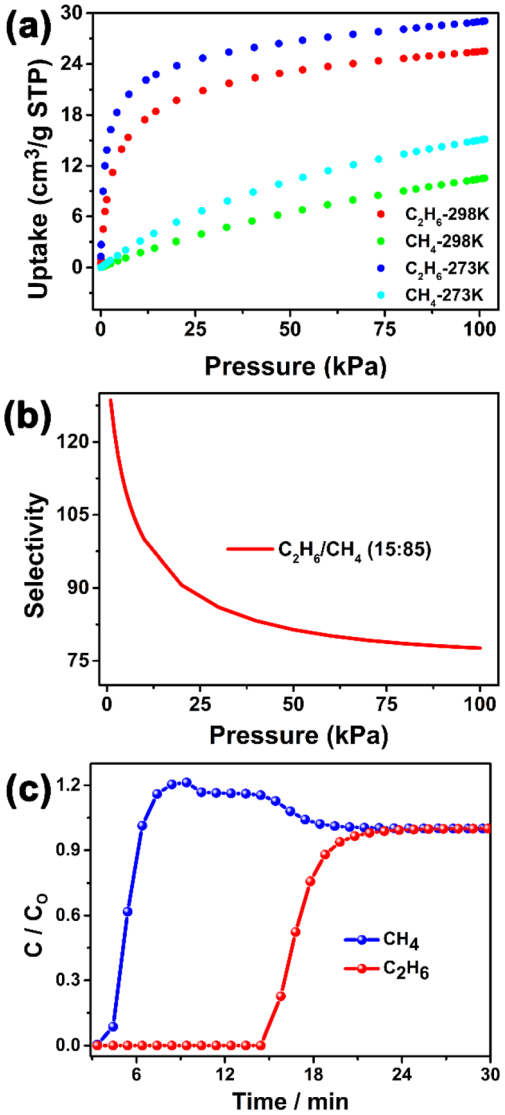

Fig. 2 Sorption isotherms of **1a** for C_2H_6 and CH_4 at 298 K and 273 K (a), IAST selectivity (b) and (c) breakthrough experiment of C_2H_6/CH_4 (15 : 85) at 298 K.

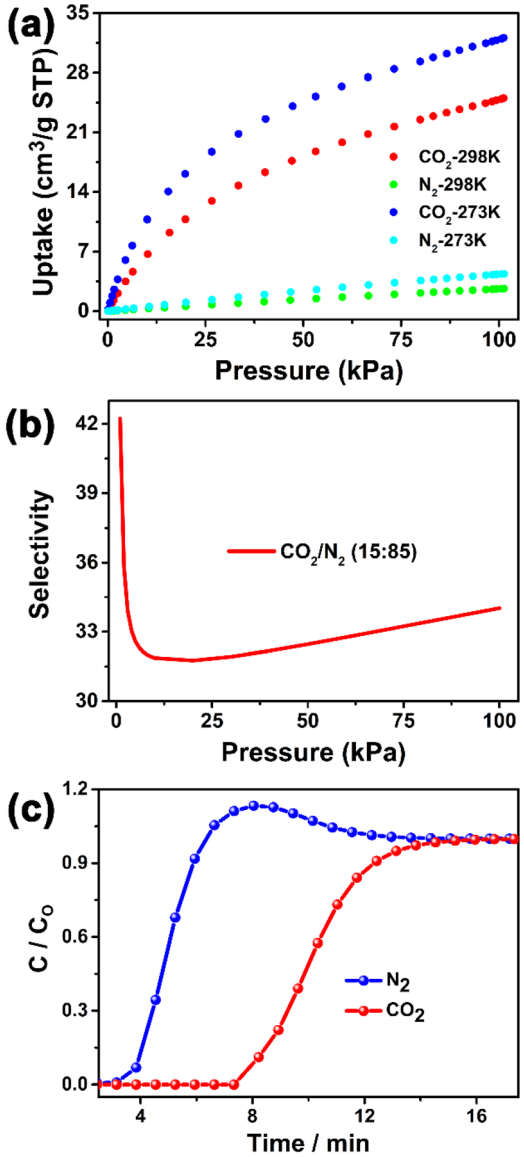

Fig. 3 Sorption isotherms of **1a** for CO_2 and N_2 at 298 K and 273 K (a), IAST selectivity (b) and (c) breakthrough experiment of CO_2/N_2 (15 : 85) at 298 K.

DMOF-Cl (12.5),[54] HOF-ZJU-201a (45) and HOF-ZJU-202a (36),[55] Ni(HBTC)(bipy) (27.5)[56] and SNNU-Bai78 (40)[57] (Table S3†). Furthermore, the good selectivity of C_2H_6/CH_4 was also proved by the breakthrough experiment (Fig. 2c). In addition, the single-component gas sorption isotherms of CO_2 and N_2 are also performed at 273 K and 298 K under 1 bar. The experiments revealed that the CO_2 uptake amount (25.0 $cm^3\ g^{-1}$) of **1a** is much higher than that of N_2 (2.7 $cm^3\ g^{-1}$) at 298 K and 1 bar (Fig. 3a), resulting an adsorption amount difference of 22.3 $cm^3\ g^{-1}$, and an CO_2/N_2 uptake ratio of 926%. Considering the large different adsorption amount and uptake ratio, we calculated the selectivity of binary mixtures of CO_2/N_2 (molar ratios: 15 : 85) at 298 K by IAST. The calculated selectivity of CO_2/N_2 is up to 34.0 at 298 K and 1 bar (Fig. 3b), which is higher than that reported for HBU-23 (28.4),[58] Eu-MOF (28.7),[59] UPC-70 (32),[60] SIFSIX-2-Cu (13.7),[61] ZIF-300 (22),[62] BUT-10 (18.6),[63] NU-1000 (8),[64] LIFM-10 (18.3),[65] MOF-5 (9)[66] and MOC-QW-3-NH_2 (23)[67] (Table S4†). Additionally, the Q_{st} value for CO_2 (23.99 kJ mol^{-1}) is higher than that of N_2 (16.03 kJ mol^{-1}), indicating a stronger framework–CO_2 interaction (Fig. S11†). Meanwhile, the good selectivity of CO_2/N_2 is further proved by the breakthrough experiment (Fig. 3c). The good selectivities of C_2H_6/CH_4 and CO_2/N_2 may be ascribed to the pore structure and the extent of interactions between the gas molecules and host framework. The above results indicate that **1a** may be a potential candidate for gas purification processes.

Additionally, luminescent Zn-MOFs as probes for the detection of metal ions have received more and more attention

because of their high sensitivity and high selectivity.[68–75] The solid state photoluminescence of **1a** was explored and it showed a high peak at 435 nm upon excitation at 365 nm and room temperature (Fig. S12†). Considering the porosity, water stability and luminescent performance of **1a**, we explored the capability of **1a** in sensing selected metal ions. Luminescence-based sensing experiments for selected metal cations were performed in an aqueous solution. 30 mg of the activated sample was soaked in 50 ml water and then ultrasonicated for 2 hours and aged for 30 min. We took 3 ml of the suspension to carry out the luminescence. After adding 100 μl of the 0.01 M metal ion aqueous solution, photoluminescence spectra were collected immediately. As shown in Fig. 4, if the luminescence intensity of **1a** in water solution was selected as the baseline, the metal ions exhibited different quenching or enhancing phenomena. Most metal ions such as Zn^{2+}, Co^{2+}, Ni^{2+}, Ag^{+}, and Fe^{2+}, showed slight fluorescence intensity variation. However, Cu^{2+}, $[Co(NH_3)_6]^{3+}$ and Fe^{3+} ions show significantly higher effects. Especially for Fe^{3+} ion, the quenching level is about 95.1%.

The above results indicate that **1a** is an especially effective sensor for detecting Fe^{3+} ions.

In order to explore the possible quenching mechanisms for Cu^{2+} and Fe^{3+} ions, we first tested the PXRD patterns of samples treated with Cu^{2+}/Fe^{3+} ions. As shown in Fig. S13,† the treated samples exhibited robust PXRD diffraction peaks, which excluded the collapse of the framework. Secondly, the UV-vis absorption spectra of Fe^{3+} ions show overlaps with the excitation and emission spectra of the Zn-MOF, suggesting that the quenching effect could be induced by competitive absorption of the excitation energy as well as fluorescence resonance energy transfer (FRET) between **1a** and Fe^{3+} ions (Fig. S14†). Compared with Fe^{3+} ions, there is negligible overlap between the UV-vis absorption spectrum of Cu^{2+} ion and the excitation and emission spectra of **1a**, which rules out the energy absorption competition and energy transfer mechanisms (Fig. S14†). Lastly, we carry out the X-ray photoelectron spectroscopy (XPS) spectra for the original sample and treated sample. Compared with the original sample, the Cu 2p and Fe 2p peaks are observed for the sample treated with Cu^{2+}/Fe^{3+} ions, respectively, indicating the existence of weak interactions between Cu^{2+}/Fe^{3+} ions and the framework (Fig. S15†). Furthermore, the high-resolution XPS spectra show that the S 2p peaks are shifted to higher binding energy after treatment with Cu^{2+}/Fe^{3+} ions, implying an electron transfer from S to Cu^{2+}/Fe^{3+} ions (Fig. S16†). Therefore, the quenching mechanisms for Cu^{2+} could be attributed to electron transfer caused by weak interactions between the Cu^{2+} and tcba-4F ligand, while the quenching mechanisms for Fe^{3+} could be explained due to the synergistic effects of weak interactions, competitive absorption and FRET mechanism between Fe^{3+} and the whole framework.[76,77]

In summary, a 2-fold robust 3D pillar-layered Zn-MOF with the (4,6)-connected ***fsc***-topology was successfully fabricated by using mixed ligands and a Zn_2 cluster. TGA and PXRD experiments prove that the activated sample possesses good thermal and water/solvent stability. More importantly, the activated sample exhibits high selective separation of C_2H_6/CH_4 (77.6, molar ratios: 15/85) and CO_2/N_2 (34, molar ratios: 15/85) at 298 K and 1 bar. On the other hand, the porous structure can selectively detect Cu^{2+}, $[Co(NH_3)_6]^{3+}$ and Fe^{3+} ions. The results of our work will shed light on the rational design and synthesis of new robust multifunctional MOF materials for the separation of gases and detection of metal ions in the future.

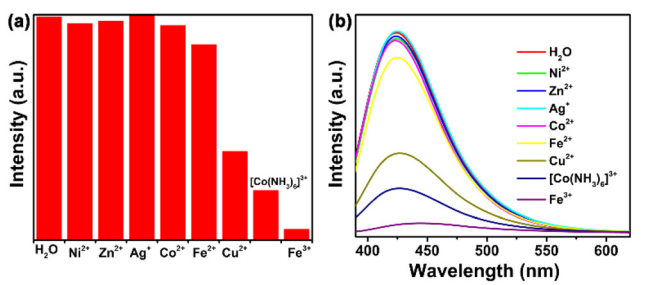

Fig. 4 (a) The maximum intensities of **1a** after adding 100 μL 0.01 M and (b) the PL spectra of $M(NO_3)_x$, $FeSO_4$ and $[Co(NH_3)_6]Cl$ loaded suspension of **1a**. Quenching percentage: Cu^{2+}: 60.3%; $[Co(NH_3)_6]^{3+}$:77.8%; Fe^{3+}: 95.1%.

Data availability

The data supporting this article have been included as part of the ESI.† Crystallographic data have been deposited at the CCDC under the accession number 2369823† and can be obtained from the CCDC website.

Conflicts of interest

There are no conflicts to declare.

Acknowledgements

This work was supported by the National Natural Science Foundation of China (no. 22201151), the Natural Science Foundation of Shandong Province (ZR2021QB078), and the Foundation of Qilu University of Technology (Shandong Academy of Sciences) Science Education Industry Integration Pilot Basic Research Project (2023PY013 and 2023PY038).

Notes and references

1 J. R. Li, R. J. Kuppler and H. C. Zhou, *Chem. Soc. Rev.*, 2009, **38**, 1477–1504.
2 H. Wu, Q. Gong, D. H. Olson and J. Li, *Chem. Rev.*, 2012, **112**, 836–868.
3 S. Yao, D. Wang, Y. Cao, G. Li, Q. Huo and Y. Liu, *J. Mater. Chem. A*, 2015, **3**, 16627–16632.

4 H. Li, K. Wang, Y. Sun, C. T. Lollar, J. Li and H.-C. Zhou, *Mater. Today*, 2018, **21**, 108–121.
5 X. Zhao, Y. Wang, D. S. Li, X. Bu and P. Feng, *Adv. Mater.*, 2018, **30**, 1705189.
6 B. R. Barnett, M. I. Gonzalez and J. R. Long, *Trends Chem.*, 2019, **1**, 159–171.
7 R.-B. Lin, S. Xiang, H. Xing, W. Zhou and B. Chen, *Coord. Chem. Rev.*, 2019, **378**, 87–103.
8 D.-X. Xue, Q. Wang and J. Bai, *Coord. Chem. Rev.*, 2019, **378**, 2–16.
9 W. G. Cui, T. L. Hu and X. H. Bu, *Adv. Mater.*, 2020, **32**, 1806445.
10 J. Li, P. M. Bhatt, J. Li, M. Eddaoudi and Y. Liu, *Adv. Mater.*, 2020, **32**, e2002563.
11 R.-B. Lin, S. Xiang, W. Zhou and B. Chen, *Chem*, 2020, **6**, 337–363.
12 H. Wang, Y. Liu and J. Li, *Adv. Mater.*, 2020, **32**, 2002603.
13 W. Fan, X. Zhang, Z. Kang, X. Liu and D. Sun, *Coord. Chem. Rev.*, 2021, **443**, 213968.
14 D. Wu, P.-F. Zhang, G.-P. Yang, L. Hou, W.-Y. Zhang, Y.-F. Han, P. Liu and Y.-Y. Wang, *Coord. Chem. Rev.*, 2021, **434**, 213709.
15 K. Chen, S. H. Mousavi, R. Singh, R. Q. Snurr, G. Li and P. A. Webley, *Chem. Soc. Rev.*, 2022, **51**, 1139–1166.
16 A. Ebadi Amooghin, H. Sanaeepur, R. Luque, H. Garcia and B. Chen, *Chem. Soc. Rev.*, 2022, **51**, 7427–7508.
17 S.-Q. Yang, L. Zhou, B. Xing, Y.-H. Zhang and T.-L. Hu, *Chin. J. Struct. Chem.*, 2023, **42**, 100004.
18 H. Yang, L. Xue, X. Yang, H. Xu and J. Gao, *Chin. J. Struct. Chem.*, 2023, **42**, 100034.
19 X. Mu, Y. Xue, M. Hu, P. Zhang, Y. Wang, H. Li, S. Li and Q. Zhai, *Chin. Chem. Lett.*, 2023, **34**, 107296.
20 K. Jiang, Y. Gao, P. Zhang, S. Lin and L. Zhang, *Chin. Chem. Lett.*, 2023, **34**, 108039.
21 Z. Di, X. Zheng, Q. Yu, H. Yuan and C.-P. Li, *Chin. J. Struct. Chem.*, 2022, **41**, 2211031–2211044.
22 F. ZareKarizi, M. Joharian and A. Morsali, *J. Mater. Chem. A*, 2018, **6**, 19288–19329.
23 Y. Ye, J. Du, L. Sun, Y. Liu, S. Wang, X. Song and Z. Liang, *Dalton Trans.*, 2020, **49**, 1135–1142.
24 K. Vellingiri, A. Deep and K. H. Kim, *ACS Appl. Mater. Interfaces*, 2016, **8**, 29835–29857.
25 Z.-P. Ni, J.-L. Liu, M. N. Hoque, W. Liu, J.-Y. Li, Y.-C. Chen and M.-L. Tong, *Coord. Chem. Rev.*, 2017, **335**, 28–43.
26 K. Otsubo, T. Haraguchi and H. Kitagawa, *Coord. Chem. Rev.*, 2017, **346**, 123–138.
27 T. Delgado, M. Meneses-Sanchez, L. Pineiro-Lopez, C. Bartual-Murgui, M. C. Munoz and J. A. Real, *Chem. Sci.*, 2018, **9**, 8446–8452.
28 C. Yu, X. Sun, L. Zou, G. Li, L. Zhang and Y. Liu, *Inorg. Chem.*, 2019, **58**, 4026–4032.
29 G. F. Hua, X. J. Xie, W. Lu and D. Li, *Dalton Trans.*, 2020, **49**, 15548–15559.
30 D. C. Mayer, J. K. ZarÈ©ba, G. Raudaschl-Sieber, A. Pöthig, M. Chołuj, R. Zaleśny, M. Samoć and R. A. Fischer, *Chem. Mater.*, 2020, **32**, 5682–5690.
31 X. J. Gao and H. G. Zheng, *Dalton Trans.*, 2021, **50**, 9310–9316.
32 A. Lancheros, S. Goswami, M. R. Mian, X. Zhang, X. Zarate, E. Schott, O. K. Farha and J. T. Hupp, *Dalton Trans.*, 2021, **50**, 2880–2890.
33 D. J. O'Hearn, A. Bajpai and M. J. Zaworotko, *Small*, 2021, **17**, e2006351.
34 J. Ha, M. Jung, J. Park, H. Oh and H. R. Moon, *ACS Appl. Mater. Interfaces*, 2022, **14**, 30946–30951.
35 J. Pei, X. W. Gu, C. C. Liang, B. Chen, B. Li and G. Qian, *J. Am. Chem. Soc.*, 2022, **144**, 3200–3209.
36 F. Hu, C. Liu, M. Wu, J. Pang, F. Jiang, D. Yuan and M. Hong, *Angew. Chem., Int. Ed.*, 2017, **56**, 2101–2104.
37 F. Hu, P. Huang, Z. Di, M. Wu, F. Jiang and M. Hong, *Chem. Commun.*, 2019, **55**, 10257–10260.
38 F. Hu, Z. Di, M. Wu, M. Hong and J. Li, *Cryst. Growth Des.*, 2019, **19**, 6381–6387.
39 F. Hu, Z. Di, M. Wu and J. Li, *Dalton Trans.*, 2020, **49**, 8836–8840.
40 Z. Di, C. Liu, J. Pang, C. Chen, F. Hu, D. Yuan, M. Wu and M. Hong, *Angew. Chem., Int. Ed.*, 2021, **60**, 10828–10832.
41 H. Li, Z. Ji, C. Chen, Z. Di, Y. Liu and M. Wu, *Cryst. Growth Des.*, 2021, **21**, 2277–2282.
42 H. Li, C. Liu, C. Chen, Z. Di, D. Yuan, J. Pang, W. Wei, M. Wu and M. Hong, *Angew. Chem., Int. Ed.*, 2021, **60**, 7547–7552.
43 Z. Di, C. Liu, J. Pang, S. Zou, Z. Ji, F. Hu, C. Chen, D. Yuan, M. Hong and M. Wu, *Angew. Chem., Int. Ed.*, 2022, **61**, e202210343.
44 S. Zou, Z. Di, H. Li, Y. Liu, Z. Ji, H. Li, C. Chen, M. Wu and M. Hong, *Inorg. Chem.*, 2022, **61**, 7530–7536.
45 V. A. Blatov, A. P. Shevchenko and D. M. Proserpio, *Cryst. Growth Des.*, 2014, **14**, 3576–3586.
46 A. L. Spek, *J. Appl. Crystallogr.*, 2003, **36**, 7–13.
47 L. Yan, H. T. Zheng, L. Song, Z. W. Wei, J. J. Jiang and C. Y. Su, *ACS Appl. Mater. Interfaces*, 2024, **16**, 6579–6588.
48 Y. Wang, X. Zhao, S. Han and Y. Wang, *ACS Appl. Mater. Interfaces*, 2024, **16**, 10468–10474.
49 X. Shi, Y. Zu, X. Li, T. Zhao, H. Ren and F. Sun, *Nano Res.*, 2023, **16**, 10652–10659.
50 W. Wang, X. H. Xiong, N. X. Zhu, Z. Zeng, Z. W. Wei, M. Pan, D. Fenske, J. J. Jiang and C. Y. Su, *Angew. Chem., Int. Ed.*, 2022, **61**, e202201766.
51 Y. Zhang, L. Yang, L. Wang, S. Duttwyler and H. Xing, *Angew. Chem., Int. Ed.*, 2019, **58**, 8145–8150.
52 A. M. Plonka, X. Chen, H. Wang, R. Krishna, X. Dong, D. Banerjee, W. R. Woerner, Y. Han, J. Li and J. B. Parise, *Chem. Mater.*, 2016, **28**, 1636–1646.
53 S. M. Li, H. C. Jiang, Q. L. Ni, L. C. Gui and X. J. Wang, *Dalton Trans.*, 2023, **52**, 9655–9663.
54 Z. Song, Y. Zheng, Y. Chen, Y. Cai, R. J. Wei and J. Gao, *Dalton Trans.*, 2023, **52**, 15462–15466.
55 Y. Liu, Q. Xu, L. Chen, C. Song, Q. Yang, Z. Zhang, D. Lu, Y. Yang, Q. Ren and Z. Bao, *Nano Res.*, 2022, **15**, 7695–7702.
56 P. Guo, M. Chang, T. Yan, Y. Li and D. Liu, *Chin. J. Chem. Eng.*, 2022, **42**, 10–16.

57 H. Cheng, Q. Wang, L. Meng, P. Sheng, Z. Zhang, M. Ding, Y. Gao and J. Bai, *ACS Appl. Mater. Interfaces*, 2021, **13**, 40713–40723.
58 S.-Q. Gang, Z.-Y. Liu, Y.-N. Bian, R. Wang and J.-L. Du, *Sep. Purif. Technol.*, 2024, **335**, 126153.
59 W.-M. Liao, M.-J. Wei, J.-T. Mo, P.-Y. Fu, Y.-N. Fan, M. Pan and C.-Y. Su, *Dalton Trans.*, 2019, **48**, 4489–4494.
60 X. Wang, Y. Wang, K. Lu, W. Jiang and F. Dai, *Chin. Chem. Lett.*, 2021, **32**, 1169–1172.
61 P. Nugent, Y. Belmabkhout, S. D. Burd, A. J. Cairns, R. Luebke, K. Forrest, T. Pham, S. Ma, B. Space, L. Wojtas, M. Eddaoudi and M. J. Zaworotko, *Nature*, 2013, **495**, 80–84.
62 N. T. Nguyen, H. Furukawa, F. Gandara, H. T. Nguyen, K. E. Cordova and O. M. Yaghi, *Angew. Chem., Int. Ed.*, 2014, **53**, 10645–10648.
63 B. Wang, H. Huang, X. L. Lv, Y. Xie, M. Li and J. R. Li, *Inorg. Chem.*, 2014, **53**, 9254–9259.
64 R. J. Li, M. Li, X. P. Zhou, D. Li and M. O'Keeffe, *Chem. Commun.*, 2014, **50**, 4047–4049.
65 Y. Xiong, Y. Z. Fan, R. Yang, S. Chen, M. Pan, J. J. Jiang and C. Y. Su, *Chem. Commun.*, 2014, **50**, 14631–14634.
66 N. Ding, H. Li, X. Feng, Q. Wang, S. Wang, L. Ma, J. Zhou and B. Wang, *J. Am. Chem. Soc.*, 2016, **138**, 10100–10103.
67 L.-Z. Qin, X.-H. Xiong, S.-H. Wang, L.-L. Meng, T.-A. Yan, J. Chen, N.-X. Zhu, D.-H. Liu and Z.-W. Wei, *Inorg. Chem.*, 2021, **60**, 17440–17444.
68 S. Kamal, M. Khalid, M. S. Khan and M. Shahid, *Coord. Chem. Rev.*, 2023, **474**, 214859.
69 K. Arya, A. Kumar, S. Mehra, Divya, A. Kumar, S. Kumar Mehta and R. Kataria, *Sep. Purif. Technol.*, 2023, **307**, 122551.
70 G. L. Yang, X. L. Jiang, H. Xu and B. Zhao, *Small*, 2021, **17**, e2005327.
71 J. Jin, J. Xue, Y. Liu, G. Yang and Y. Y. Wang, *Dalton Trans.*, 2021, **50**, 1950–1972.
72 S. A. A. Razavi and A. Morsali, *Coord. Chem. Rev.*, 2020, **415**, 213299.
73 B. B. Rath and J. J. Vittal, *Inorg. Chem.*, 2020, **59**, 8818–8826.
74 A. Mandal, A. Adhikary, A. Sarkar and D. Das, *Inorg. Chem.*, 2020, **59**, 17758–17765.
75 S. K. Panda, S. Mishra and A. K. Singh, *Dalton Trans.*, 2021, **50**, 7139–7155.
76 Y. Du, H. Yang, R. Liu, C. Shao and L. Yang, *Dalton Trans.*, 2020, **49**, 13003–13016.
77 J. Pang, R. Du, X. Lian, Z.-Q. Yao, J. Xu and X. Bu, *Chin. Chem. Lett.*, 2021, **32**, 2443–2447.